Design and Comparison of High-speeds PMSM and IM for Aircraft Application

Dahnoun Larbi
GREEN and Electrical and Electronic Systems Research Group
Université de Lorraine and SAFRAN Tech
Nancy and Magny-les-Hameaux, France
larbi.dahnoun@univ-lorraine.fr

Fontchastagner Julien, Mezani Smaïl, Takorabet Noureddine
Université de Lorraine, GREEN
Nancy, France
julien.fontchastagner@univ-lorraine.fr
smail.mezani@univ-lorraine.fr
noureddine.takorabet@univ-lorraine.fr

Viguier Christophe
Electrical and Electronic Systems Research Group
SAFRAN Tech
Blagnac, France
christophe.viguier2@safrangroup.com

Abstract—**The recent increase in aircraft electrical energy requirements leads to investigate more efficient topologies for on-board electrical generation. This paper present analytical models for the electromagnetic and mechanical design of a PMSM and an IM operating at high-speed levels. The designed machines will be compared in order to study the best solution mainly regarding power density for the application.**

Keywords—high-speed machine, analytical models, on-board power generation, permanent magnet machine, induction machine.

I. Introduction

In recent years, the trend towards electrification of different systems has emerged in the aviation industry, setting new challenges for hybrid aviation in terms of embedded power generation system topologies. The traditional three-stage topology with a Permanent Magnet Generator (PMG), an exciter connected to the wound rotor synchronous generator by a rotating diode bridge rectifier, although robust and widely used, must be renewed in order to reach higher power densities. Studies are being carried out to lighten the structure by proposing direct-drive generators on the turbojet reactor in order to tend towards high-speed systems. Thus, the increase in the operating speed of the machine makes it possible to reach interesting power densities but is also synonymous with many considerations regarding the mechanical behavior of the entire rotating system. The track of the permanent magnet generators is under study and allows to obtain the first products capable of operating at nearly 40 krpm while supplying hundreds of kilowatts. The purpose of the work is to study two topologies of high-speed generators by considering their magnetic and mechanical design. Discussions will be held to determine the most appropriate technology for an aeronautical application.

II. Context

In [1], the authors draw a global overview of the different topologies of generators developed and tested for aircraft power generation. It is shown for speeds below 35 krpm, the most used topology will be the wound-field synchronous machine and for higher power densities it will be the permanent magnet synchronous machine (PMSM). But above 35 krpm, the most used topologies will be the ones with solid rotor like induction machine (IM), or switched reluctance machine (SRM) while it remains a few applications with PMSM. Thus, the purpose of this work is to set a comparative study between the PMSM and an IM for aircraft power generation application.
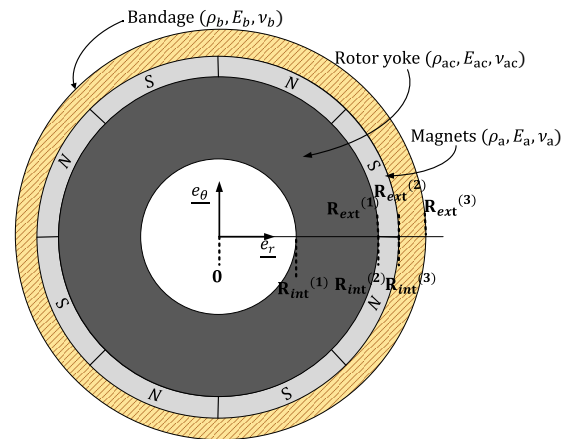
III. Model of the PMSM

Fig. 1. Schematic representation of a PMSM rotor

In this type of high speed PMSM, it is important to properly size the sleeve so that it remains a contact between the magnets and the rotor yoke. Reference [2] shows that different analytical approaches exists in the literature to evaluate the stresses caused by the centrifugal effects and the forced fit bandage in the rotor. It is shown that the displacement method, developed by [3], is the most suitable and effective method. Considering the three concentric cylinders on Fig. 1, modelling each layer of the PMSM, one can calculate the displacements of each external surface of the cylinders as following:

$$
\begin{cases}
u^{(1)}\left(r = R_{ext}^{(1)}\right) = \frac{2.(3+\nu_{ac}).\rho_{ac}.\omega^2.R_{ext}^{(1)\,3}}{8.E_{ac}} \cdot \left(\frac{1-\nu_{ac}}{3+\nu_{ac}} + \left(\frac{R_{int}^{(1)}}{R_{ext}^{(1)}}\right)^2\right) \\[2.5ex]
u^{(2)}\left(r = R_{int}^{(2)}\right) = \frac{2.(3+\nu_{a}).\rho_{a}.\omega^2.R_{ext}^{(2)\,2}.R_{int}^{(2)}}{8.E_{a}} \cdot \left(1 + \frac{1-\nu_{a}}{3+\nu_{a}} \cdot \left(\frac{R_{int}^{(2)}}{R_{ext}^{(2)}}\right)^2\right) \\[2.5ex]
u^{(2)}\left(r = R_{ext}^{(2)}\right) = \frac{2.(3+\nu_{a}).\rho_{a}.\omega^2.R_{ext}^{(2)\,3}}{8.E_{a}} \cdot \left(\frac{1-\nu_{a}}{3+\nu_{a}} + \left(\frac{R_{int}^{(2)}}{R_{ext}^{(2)}}\right)^2\right) \\[2.5ex]
u^{(3)}\left(r = R_{int}^{(3)}\right) = \frac{2.(3+\nu_{f}).\rho_{f}.\omega^2.R_{ext}^{(3)\,2}.R_{int}^{(3)}}{8.E_{f}} \cdot \left(1 + \frac{1-\nu_{f}}{3+\nu_{f}} \cdot \left(\frac{R_{int}^{(3)}}{R_{ext}^{(3)}}\right)^2\right)
\end{cases}
\tag{1}
$$

With, $\nu_{ac,a,f}$ the Poisson's ratio of steel, magnet and bandage,
$E_{ac,a,f}$ the Young's modulus of steel, magnet and bandage,
$\rho_{ac,a,f}$ the density of steel, magnet and bandage.

Then it is possible to express the mechanical interferences $e^{(1,2)}$ and $e^{(2,3)}$ at the interfaces, defined as the differences between the displacement of the internal face of the upper layers and the displacement of the external face of the lower layers.

$$\begin{cases} e^{(1,2)} = u^{(2)}\left(r = R_{int}^{(2)}\right) - u^{(1)}\left(r = R_{ext}^{(1)}\right) \\ e^{(2,3)} = u^{(3)}\left(r = R_{int}^{(3)}\right) - u^{(2)}\left(r = R_{ext}^{(2)}\right) \end{cases} \quad (2)$$

These interferences must remain null to ensure the contact between the different layers of the rotor during its operation. Thus, pressures at each boundary can be find and as only the bandage will be in reality highly pre-stressed, it is possible to identify the resulting pressure at its interface as well as the stresses within it.

$$\begin{cases} \sigma_{rr}\left(r = R_{int}^{(3)}\right) = -p_2' \\ \sigma_{\theta\theta}\left(r = R_{int}^{(3)}\right) = \frac{(3+\vartheta_f)}{8} \cdot \rho_f \cdot \omega^2 \cdot \left(R_{int}^{(3)^2}\left(1 - \frac{1+3.\vartheta_f}{3+\vartheta_f}\right) + 2.R_{ext}^{(3)^2}\right) \\ \qquad -p_2'\left(1 + 2.\frac{R_{ext}^{(3)^2}}{R_{int}^{(3)^2} - R_{ext}^{(3)^2}}\right) \end{cases} \quad (3)$$

From the expression of the stresses in the sleeve, an equivalent stress is formulated and will allow the comparison with the material yield strength of the sleeve. For the case of isotropic metallic materials, the Von Misses equivalent stress is commonly used and can be expressed from $\sigma_{rr}, \sigma_{\theta\theta}, \sigma_{zz}$, respectively the stresses in the three direction of the space (4).

$$\sigma_{VM} = \frac{1}{\sqrt{2}}\sqrt{(\sigma_{rr} - \sigma_{\theta\theta})^2 + (\sigma_{\theta\theta} - \sigma_{zz})^2 + (\sigma_{zz} - \sigma_{rr})^2} \quad (4)$$

For the electromagnetic design of the PMSP, a classical approach based on [4], [5] is used. This approach is first based on the evaluation of the volume of the rotor to reach nominal power established in the requirements. During this first step, induction in the airgap is calculated thanks to the magnetic properties of the magnets, their volume and the airgap. Then winding, the number of turns, current and cross section area can be calculated thanks to the expression of the airgap flux and its conservation and also the current densities. Finally, the lamination dimensions which allows to determine the width of the flux paths in the machine are calculated by imposing induction limits within these different regions (Fig. 2). The validation of the model is done thanks to finite element simulations on Flux2D.
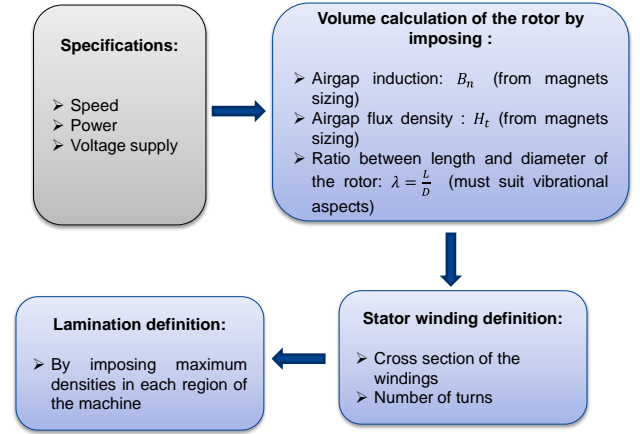

Fig. 2. Steps for the sizing of PMSM

IV. PRESENTATION OF THE IM

The IM which will be here investigated is specifically designed to ensure high-speed operations. The rotor is composed of three layers, respectively the layer corresponding to the shaft, another corresponding to the rotor yoke and a final one corresponding to a copper ring. This kind of IM has been well investigated upon the literature [6], [7] and many prototypes has been built [8]. Thanks to the perfectly orthoradial symmetry of the rotor, the machine can reach peripherical speeds above 200 m.s⁻¹. However, this architecture of rotor is only possible if special attention is made to the interface between the copper ring and the rotor yoke so that the contact remains even at high-speed levels.

A. Calculation of rotor parameters in the magnetic model

For the electromagnetic design of the machine, the study can be based on the establishment of an equivalent single-phase electrical circuit in which the value of the various components will depend directly on the parameters of the machine [5], [9]–[11]. To determine the rotor parameters on the equivalent electrical circuit a specific approach is needed as there are no cage at the rotor. An analytical approach by considering one half of rotor pole (Fig. 3) is used. Then, the aim is to identify the expression of the current density within the copper ring which is in the half rotor pole and supposed to be in the same direction. Moreover, thanks to Maxwell's equations it is possible to find the repartition of the magnetic field in the copper ring and by the way the expressions of the rotor resistance and leakage inductance considering skin effects.
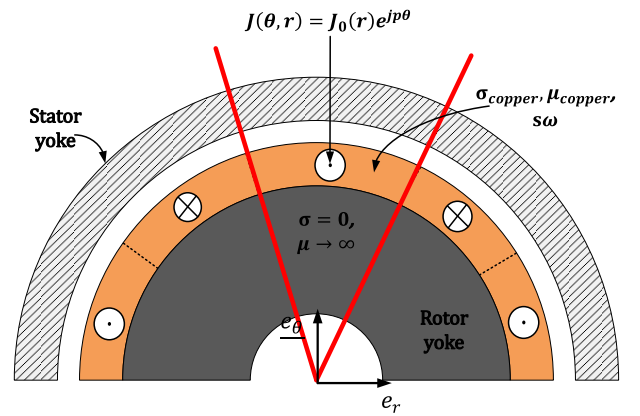

Fig. 3. Schematic representation of the IM for the calculation of its rotor parameters

B. Mechanical model for multi-layer rotor

One of the mechanical analytical model approaches developed in [2] is used by extending the study to a multilayer rotor. A long rotor consisting in a succession of layers of different materials is considered (Fig. 4). Considering a long rotor, a conventional approach called plane deformations is initiated, modelling the fact that the rotor sections are far enough from the edges so that they remain flat under centrifugal effects. It is then possible to write:

$$\begin{cases} \varepsilon_{rr} = \dfrac{1}{E}\left(\sigma_{rr} - \nu(\sigma_{\theta\theta} + \sigma_{zz})\right) \\ \varepsilon_{\theta\theta} = \dfrac{1}{E}\left(\sigma_{\theta\theta} - \nu(\sigma_{rr} + \sigma_{zz})\right) \\ \qquad \varepsilon_{zz} = 0 \end{cases} \quad (5)$$

With: $\underline{\varepsilon}$ the strain tensor,

$\underline{\sigma}$ the stress tensor,

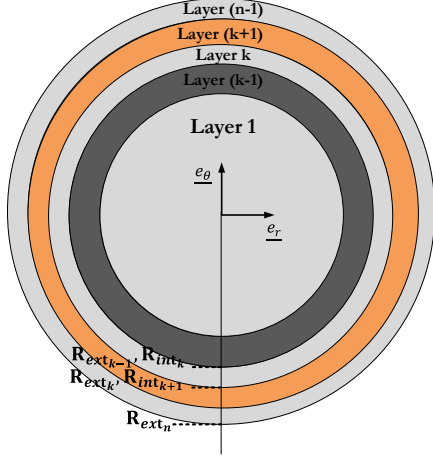E, ν Young's modulus and Poisson's ratio.

Fig. 4. Schematic representation of a multilayered rotor

Using the isotropic linear elasticity law and making the hypothesis of small disturbances, the expression of constraints in the three directions of space can then be put in the form:

$$\begin{cases} \sigma_{rr} = (\lambda + 2\mu)\dfrac{\partial u_r}{\partial r} + \lambda\left(\dfrac{u_r}{r} + \epsilon_{zz}\right) \\ \sigma_{\theta\theta} = (\lambda + 2\mu)\dfrac{u_r}{r} + \lambda\left(\dfrac{\partial u_r}{\partial r} + \epsilon_{zz}\right) \\ \sigma_{zz} = (\lambda + 2\mu)\epsilon_{zz} + \lambda\left(\dfrac{\partial u_r}{\partial r} + \dfrac{u_r}{r}\right) \end{cases} \quad (6)$$

With: $\underline{u}$ the displacement field,

λ, μ, Lamé's parameters.

By applying the fundamental principle of dynamics (7), we obtain an equation with partial derivatives (8), whose solution can be put in the form (9).

$$\underline{\mathrm{div}}\left(\underline{\sigma}\right) + \rho\underline{f} = 0 \quad (7)$$

$$\frac{\partial^2 u_r}{\partial r^2} + \frac{1}{r}\frac{\partial}{\partial r}(u_r) - \frac{u_r}{r^2} = -\frac{\rho\omega^2}{\lambda + 2\mu}r \quad (8)$$

$$\begin{cases} u_r(r) = -\dfrac{\rho\omega^2}{8(\lambda + 2\mu)}r^3 + K_1 r + \dfrac{K_2}{r} \\ \sigma_{rr} = -\dfrac{\rho\omega^2}{8(\lambda + 2\mu)}r^2(4\lambda + 6\mu) + K_1(2\lambda + 2\mu) - \dfrac{K_2}{r^2}2\mu \end{cases} \quad (9)$$

With: ρ the material density,

$\underline{f}$ the volume forces induced by the speed of rotation that can be written as $\underline{f} = r\omega^2 \underline{e}_r$,

ω the rotation speed.

In order to obtain the evolution of the stresses in the rotor it will then be necessary to identify the unknowns of (9) by using the boundary and continuity conditions of the different physical quantities of the system under study. It is first possible to state that K_2 of the first layer is null for physical reasons ($u_{r_1}(0) \neq \infty$). Moreover, it is necessary to model the fact that the external surface of the rotor is in open air, that the displacement at the interfaces will be the same for the two adjacent layers, and according to the principle of action-reaction, the radial stress will be transmitted from layer to layer. Thus, for the layer k of the rotor:

$$\sigma_{rr_n}\left(R_{ext_n}\right) = 0$$

$$\sigma_{rr_k}\left(R_{ext_k}\right) = \sigma_{rr_{k+1}}\left(R_{int_{k+1}}\right) \qquad \text{k=1...n-1}$$

$$u_{rr_k}\left(R_{ext_k}\right) = u_{rr_{k+1}}\left(R_{int_{k+1}}\right) \qquad \text{k=1...n-1}$$

$$u_{rr_1}(0) \neq \infty \qquad (10)$$

By simulating this system, it can be observed that the radial stress is positive as it is possible to intuit it, reflecting the centrifugal effects applied on the different layers. On the other hand, by simulating the same finite element system, we observe that stress breaks will take place at each interface reflecting the fact that a tensile radial stress exists between the different layers symbolizing the forces of the lower layers on the upper layers and this is accentuated when the rotation speed of the system increases.

In order to account for this tensile stress in the analytical model, it is necessary to review the hypothesis of the transmission of displacements, since it is in fact necessary to introduce a difference between the outer radius of the lower layers and the inner radius of the upper layers thus preventing the rotor layers from separating at high speed and allowing a transmission of the tensile radial stress. We then have:

$$R_{ext_k} + u_{r_k}\left(R_{ext_k}\right) = R_{int_{k+1}} + u_{r_{k+1}}\left(R_{int_{k+1}}\right) \quad (11)$$

Thus, it is possible to see (Fig. 5) that now the results from the analytical model coincide very well with those from the FE with less than 6% error for the case of a rotor consisting of 5 layers, respectively of iron and stainless steel, iron, copper and a last layer of iron.
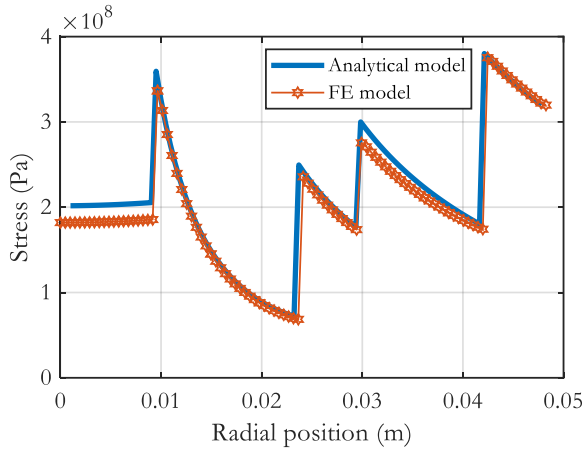
Fig. 5. Evolution of the Von Misses stress in a rotor consisting of 5 layers without separation at high speed

The radial position is equal to zero for the center of the rotor and is equal to the outer radius when at the extremity of the rotor.

V. DESIGN PROCESS AND DISCUSSION OF THE RESULTS

Now that the models have been developed and verified thanks to finite element simulations, it is possible to design the PMSM and the IM for a generation of 300kW at a nominal speed of 40 krpm. First the electromagnetic model of each machine is used to determine the stator and the copper ring geometry in the case of the IM and the magnets and rotor geometry in the case of the PMSM. Then thanks to the mechanical model, it is possible to determine the right copper ring radius and thickness to ensure the mechanical handling of the rotor in the case of the IM and the sleeve thickness in the case of the PMSM. Finally, the obtained design of machine is simulated to verify that the magnetic constraints defined in the specifications are satisfied. If it is not the case the process is reissued by changing copper ring geometry for IM or magnets and rotor geometry for the PMSM.
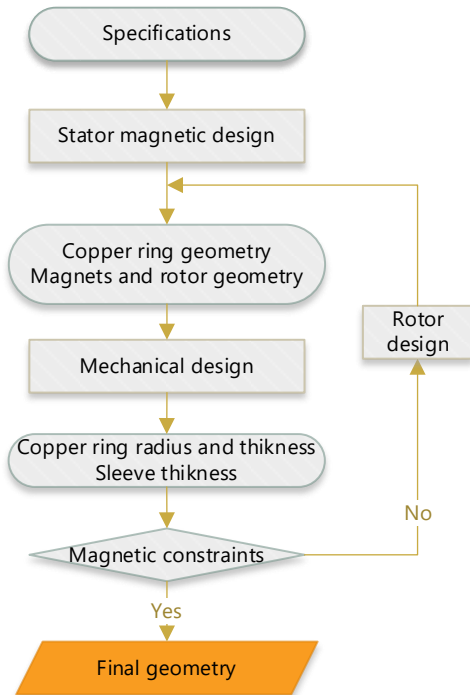

Fig. 6. Flowchart of the design process of the two high-speed machines

Applying the design process to the specifications previously presented leads to two final designs which can reach a nominal speed of 40 krpm in safe conditions. The design of the PMSM obtained is shown in Fig. 7, and is composed of a four-pole machine with neodymium magnets (1.19T of residual induction) in a total volume of machine of 3.9dm^3.
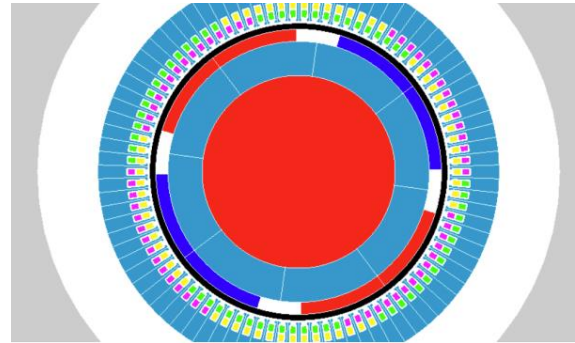

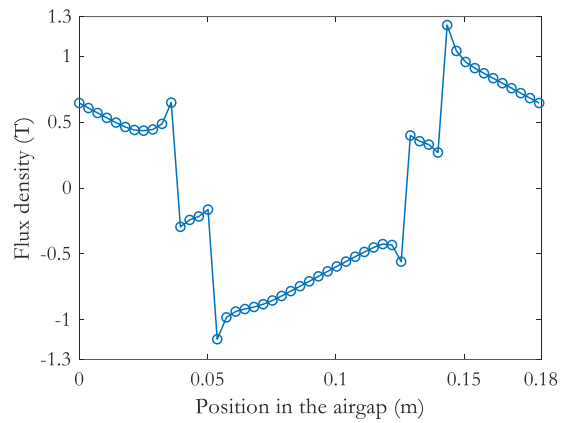Fig. 7. Result of the design of the PMSM
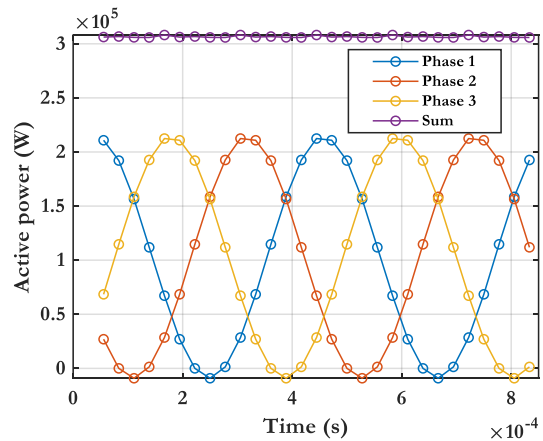

Fig. 8. Evolution of the airgap flux density

Fig. 9. Evolution of the output active power of the machine

Use of the developed mechanical model to design de sleeve thickness allows to find that the carbon fiber sleeve needs to be 2.6mm so that the contact between the magnets and the rotor yoke is ensured. A characterization of the performance of the designed machine is done thanks to the finite element software Flux2d. It can be shown on Fig. 8 that the airgap flux density is around 0.7T as it was set in the magnetic design process. Also, a simulation of a transient

application is done by feeding the machine with a 126A current source. It is found on Fig. 9 that the active power generated by the stator winding is around 210kW for each phase and leads to provide the 300kW of total output power when adding each phase power.

For the case of the induction machine the same design process is followed. The rotor is now composed of two layers and the contact between each of them is ensured thanks to a specific technique of welding that allows to merge at a microscopic level the copper ring to the rotor yoke. Nevertheless, the stress still needs to be kept under the yield strength of each material to ensure mechanical handling
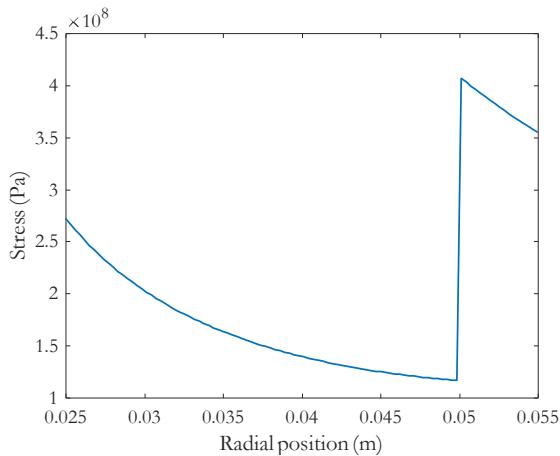

Fig. 10. Evolution of Von Misses stress in the induction machine rotor with a copper ring

A rotor of 55mm of radius with a copper ring of 5mm thickness is simulated thanks to the analytical mechanical model and it is shown on Fig. 10 that it suits the restrictions as the stress is less than 430 MPa along the copper ring.

The magnetic design of the machine allows to propose a two-pole machine with a volume of $13.3 dm^3$. It is important to notice that the thickness of the copper ring has two opposite effects on the performance of the machine. In one way increasing this thickness allows to induce a non-concentrated current in the rotor with conceivable current densities thus providing a good coupling between stator and rotor. In the other way it will also increase the airgap because of copper magnetic properties.

Giving this design, a finite element model of the machine using FEMM software is done by setting all the characteristics of the material, the windage and geometry (Fig. 11).
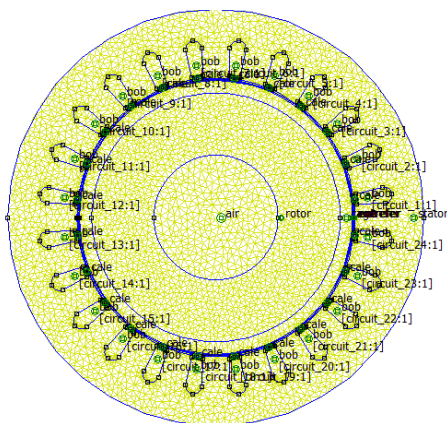

Fig. 11. Result of the design of the IM

The results of the output torque depending on the slip are shown in Fig. 12. It is possible to observe that the required torque of approximately 75N.m is reach for a slip of 0.5%.
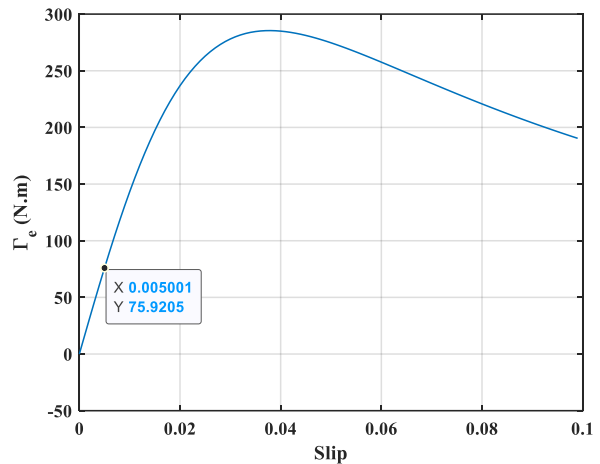

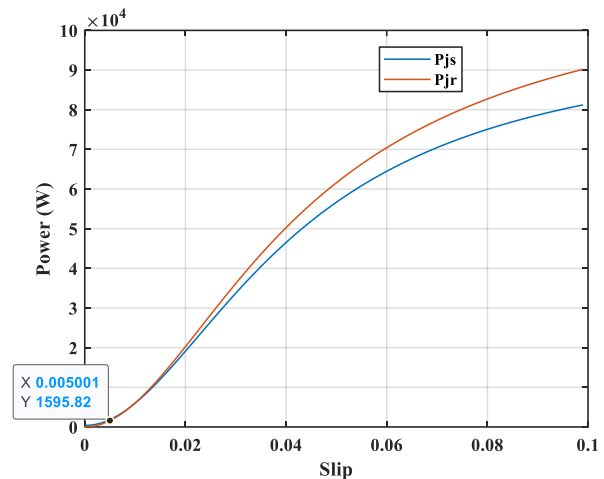Fig. 12. Evolution of the output torque of the designed induction machine depending on the slip

Fig. 13. Evolution of rotor and stator Joule losses depending on the slip

The previous figure allows to present the evolution of the Joule losses in the stator and in the rotor. In order to minimize those losses, it is important to keep the machine in the low range slip as those losses will significantly increase when increasing the slip.
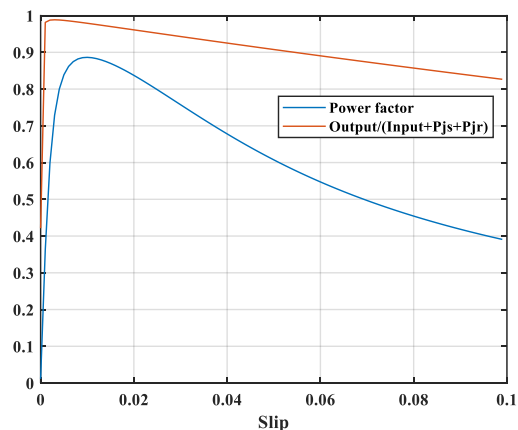

Fig. 14. Evolution of two performance ratio of the induction machine depending on the slip

Fig. 14 shows the evolution of two different parameters of the induction machine. The first one is the ratio between the output power and the sum between the absorbed power and Joule losses. This ratio is very high showing that the output power is much greater than the losses calculated in the model. However, one has to notice that this ration is not the efficiency of the machine as for example the iron losses are not included. The same remark can be done for the second ration shown on Fig. 14 as the iron losses has an impact on the power factor of the machine.

The results previously shown comes from a 2D finite element model and when simulating the same machine in a 3D finite element software different performance are find. The reason of this can be explained by the visualization of the current density distribution in one half of the cooper ring.
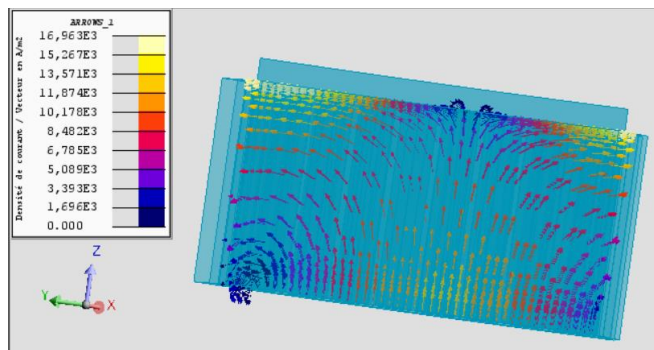

Fig. 15. Current density in the axial length of the copper bar (3D model)

It is possible to see that current loops in the copper ring axial length are developing themselves under the action of the magnetic field. Those loops have an important impact on the performances of the machine and are partially taken into account in the 2D model by implementing an equivalent resistivity of the copper ring calculated as following:

$$\rho_{eq} = \rho_{copper} \frac{2(L_z + \tau_p)}{L_z} \qquad (12)$$

With:

ρ_{copper} the electric resistivity of the copper,
L_z the axial length of the copper ring,
τ_p the length of the return loop (in y direction).

Moreover, a thermal study of the designed induction machine needs to be done in front of the important Joule losses located in the rotor which will significantly impact the performances.

VI. CONCLUSION

The presented work allows to develop an analytical way to design two type of high-speed machines. The process considers the electromagnetic aspects as well as the mechanical ones to ensure safety conditions of operation. It has been shown that the PMSM allows to reach four times much higher power densities comparing with the induction machine. However, in certain applications such as electrical

generation on aircrafts, high level of robustness and safety is needed. Thus magnet-free alternatives can be preferred specifically at high speed levels as the excitability of the machine will naturally be shut down in case of stator short-circuit default for example. It has also been shown that for the case of the induction machine a 3D study is preferable to fully demonstrate the potential of this topology and correctly take into account complex 3D phenomena which has a strong impact on the performances.

VII. AKNOWLEDGMENT

REFERENCES

[1] Y. Wang, S. Nuzzo, H. Zhang, W. Zhao, C. Gerada, and M. Galea, 'Challenges and Opportunities for Wound Field Synchronous Generators in Future More Electric Aircraft', *IEEE Transactions on Transportation Electrification*, vol. 6, no. 4, pp. 1466–1477, Dec. 2020, doi: 10.1109/TTE.2020.2980189.

[2] L. Dahnoun *et al.*, 'Comparison Of Methods For Evaluating Mechanical Stress In The Rotor Of High-Speed Machines', in *2022 International Conference on Electrical Machines (ICEM)*, Sep. 2022, pp. 752–759. doi: 10.1109/ICEM51905.2022.9910837.

[3] G. Spinnler, 'Conception des machines: principes et applications (vol. 3) - Dimensionnement - Georges Spinnler (EAN13 : 9782880743031)', *EPFL Press*.

[4] J. Pyrhonen, T. Jokinen, and V. Hrabovcová, *Design of rotating electrical machines*. Chichester, West Sussex, United Kingdom ; Hoboken, NJ: Wiley, 2008.

[5] B. Laporte, *Machines électriques tournantes : Conception, dimensionnement, fonctionnement*. Paris: ELLIPSES, 2007.

[6] J. Pyrhönen, J. Nerg, P. Kurronen, and U. Lauber, 'High-Speed High-Output Solid-Rotor Induction-Motor Technology for Gas Compression', *Industrial Electronics, IEEE Transactions on*, vol. 57, pp. 272–280, Feb. 2010, doi: 10.1109/TIE.2009.2021595.

[7] V. Bilek, J. Barta, P. Losak, I. Lolova, M. Kroupa, and G. Bramerdorfer, 'Design of Modular High-Speed Copper Coated Solid Rotor Induction Machine', in *2022 International Conference on Electrical Machines (ICEM)*, Sep. 2022, pp. 760–766. doi: 10.1109/ICEM51905.2022.9910743.

[8] V. Poumarede, S. Beddock, F. Mercier-Calvairac, and T. Klonowski, 'Electrical Hybridization of a Rotorcraft Gas Turbine Engine', presented at the MEA 2017, Bordeaux, France, Feb. 2017.

[9] Saint-Michel and Manfé, *Moteur asynchrone triphasé - Eléments de calcul*, Fév-91.

[10] I. Boldea and S. A. Nasar, *The induction machine handbook*. in Electric power engineering series. Boca Raton: CRC Press, 2002.

[11] R.-P. Bouchard and G. Olivier, *Conception de moteurs asynchrones triphasés*. éd. de l'Ecole Polytechnique de Montréal, 1997.